

# **Mercury's DEM and FAG fractal structure – indicator for meteorite bombardment by different density space bodies**

*Boyko Rangelov<sup>1</sup>, Rosen Iliev<sup>2</sup>*

<sup>1</sup>University of Mining and Geology “St. Ivan Rilski” Faculty of Geology Exploration Department of Applied Geophysics, Sofia, Bulgaria

<sup>2</sup>Institute for Space Research and Technology, Bulgarian Academy of Sciences, Sofia, Bulgaria

**Abstract.** Over the past few decades Messenger spacecraft missions have provided to the scientific community a huge amount of new data on the geology and physics of the planet closest to the Sun – Mercury. The collected data became the starting material for the building of the gravity field model of the Mercury – HgM008. Based on it, a very recent NASA scientific team has released a high-quality “free-air” gravity map for the topography of the small planet. This enables new analyzes and interpretations of Mercury’s physics and geology. The present study presents the results of Mercury’s free-air gravity field (FAG) and digital elevation model (DEM) analysis using the (multi)fractal approach. The obtained results shed new light on the natural processes that have taken place during the geological evolution of Mercury. The results confirmed clear differences between the two hemispheres of the

planet. Within the northern hemisphere fractal dimensions of FAG and DEM have variations ( $R^2$ ) 0.908 and 0.942, while within the southern hemisphere  $R^2$  of FAG and DEM have values 0.975 and 0.857. The results obtained determine the different intensity and density characteristics of space objects colliding with Mercury's two hemispheres, which necessitates additional interpretations.

## Methods and Data

### Fractal Dimension Estimation

In the present study the fractal analysis is performed using fractal surface approach. Based on the variogram [*Mark and Aronson*, 1984], the fractal calculator (FocallD) generates an image through a window around each raster pixel. In this way the fractal calculator initially estimates a variogram, and

$$y(h) = \text{Var}(Z_i - Z_j)$$

where  $i, j$  are spaced by the distance vector  $h$ . Then derived by regressing the logarithm of the distance vector with the logarithm of the variance [*Zhou and Lam*, 2005] is calculated the slope of regression. Finally, the

fractal dimension ( $D$ ) is estimated through the following formula:

$$D = 3 - (B/2)$$

where  $D$  is fractal dimension and  $B$  is the slope of the regression.

The fractal value of each pixel reflects the variation complexity [*Pentland*, 1984] of the gravity field or topography. The fractal signal value is much higher, when elevation or gravity values have a more complex variation in regard to their neighboring pixel cells.

## Data and Software

The analysis of the Mercury's "free-air" gravity anomalies was performed using data (in GMT format) from the recently released Hermean (HgM008) gravity field model [*Genova et al.*, 2019]. Input data derived from MESSENGER (Mercury Surface, Space Environment, Geochemistry and Ranging) spacecraft missions.

Mercury's topography analysis is based on data from Mercury Global Digital Elevation Model (DEM) v2 [*Becker et al.*, 2016] derived from MESSENGER space-

craft missions [*Solomon et al.*, 2001]. The DEM is created at  $665 \times 665$  m spatial resolution.

The gravity and DEM data have been processed and explored using Geographic Information System (GIS) – SAGA-GIS [*Conrad et al.*, 2015], QGIS [*Thiede et al.*, 2014] and LandSurf (Wood, J., The LandSurf Manual, <http://www.staff.city.ac.uk/jwo/landserf/landserf230/doc/landserfManual.pdf>) free software.

## **Free-Air Gravity Anomalies and Digital Elevation Model (DEM) of the Mercury**

In gravimetry, “free-air” or Faye’s gravity anomaly is an anomaly in free atmosphere calculated from the observed value of the power of the normal gravity field, reduced to the height at the point of observation. On Mercury’s topography the “free-air” gravity field reflects the elevation differences on the surface (Figure 1). The free-air gravity values are best expressed by interaction between negative (craters) and positive (mountains, ridges) landforms. For its part, the digital elevation model describes the spatial distribution and

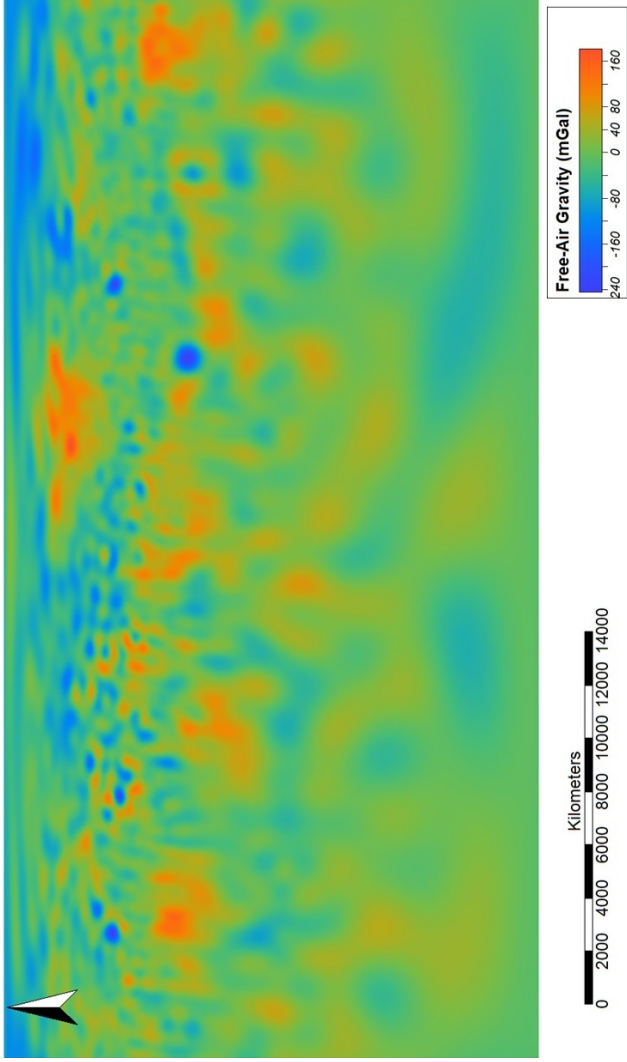


**Figure 1.** Spatial and frequency distribution of the Mercury's FAG anomalies.

interconnections of landforms.

Mercury's free-air gravity field varies from  $-227$  to  $+141$  mGals. The negative gravity anomalies dominated over the positive ones (Figure 1). Almost 55% of the total area of the gravity field is occupied by negative gravity anomalies, 40.5% of positive gravity anomalies and only 4.5% is for "normal" gravity field. As a whole the FAG is more variable within the northern hemisphere (Figure 2), than within the southern hemisphere (Figure 3) of the planet. The southern hemisphere of the planet (especially within latitudes above  $30^{\circ}$ – $35^{\circ}$ ) is entirely dominated by a negative gravity field. Within the equatorial regions of the planet (from  $0^{\circ}$  to  $25^{\circ}$  –  $30^{\circ}$  in both hemispheres), the FAG is represented by values ranging from the highest to the lowest ones.

The digital elevation model of Mercury's topography varies from  $-5272$  m to  $4273$  m (Figure 4). Negative values occupy about 60%, while the positive ones occupy about 40% of the planet's surface. Negative landforms are represented by impact craters, while the positive ones by mountains and ridges. In the northern hemisphere, the negative landforms prevail (Figure 5), while within the southern hemisphere the positive landforms are more dominant (Figure 6). Most of moun-

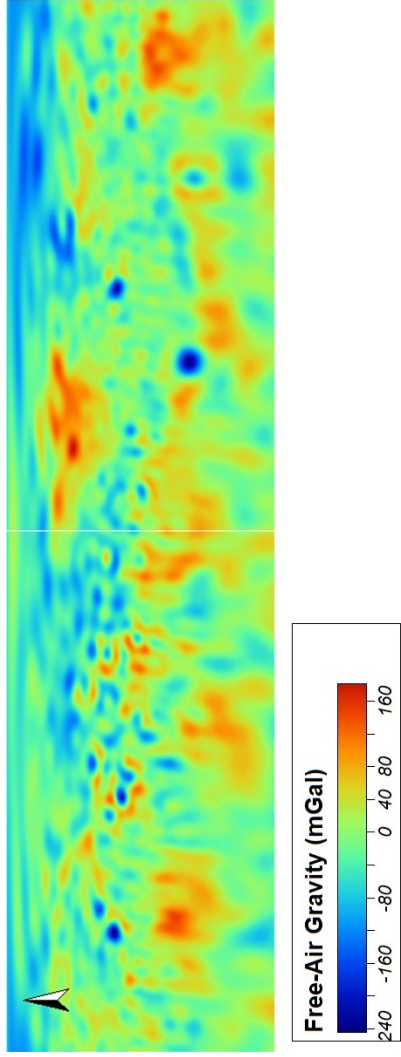


**Figure 2.** Spatial and frequency distribution of the FAG anomalies within the northern hemisphere of Mercury.

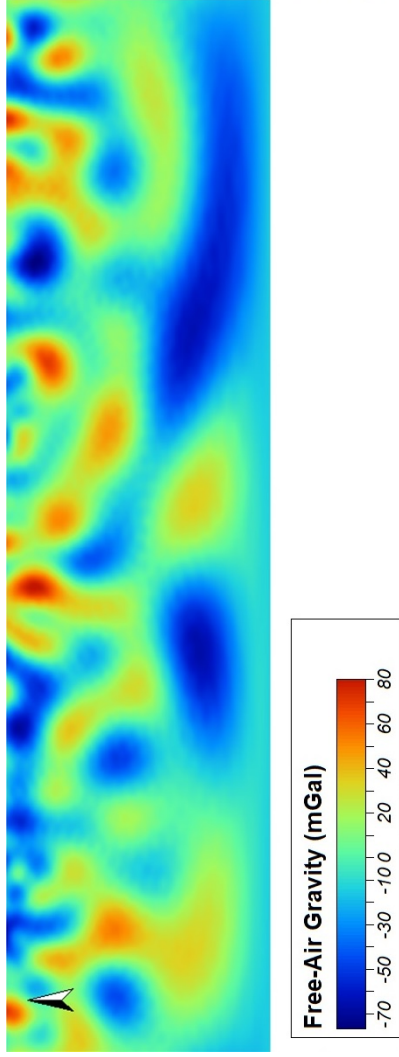


**Figure 3.** Spatial and frequency distribution of the FAG anomalies within the southern hemisphere of Mercury.

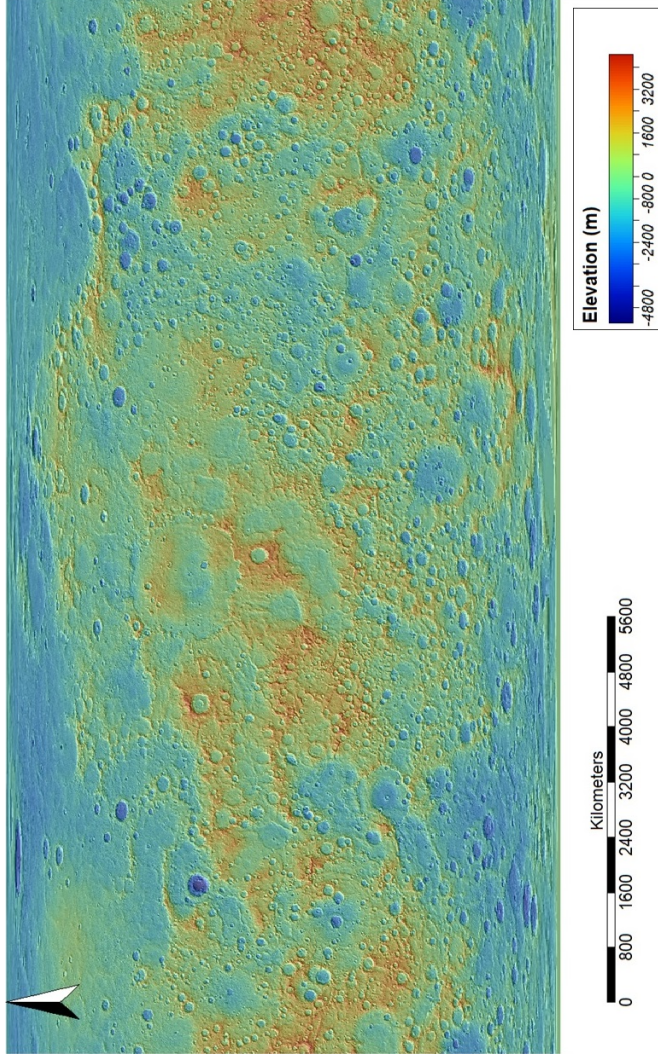


**Figure 4.** Spatial and frequency distribution of the Mercury DEM.

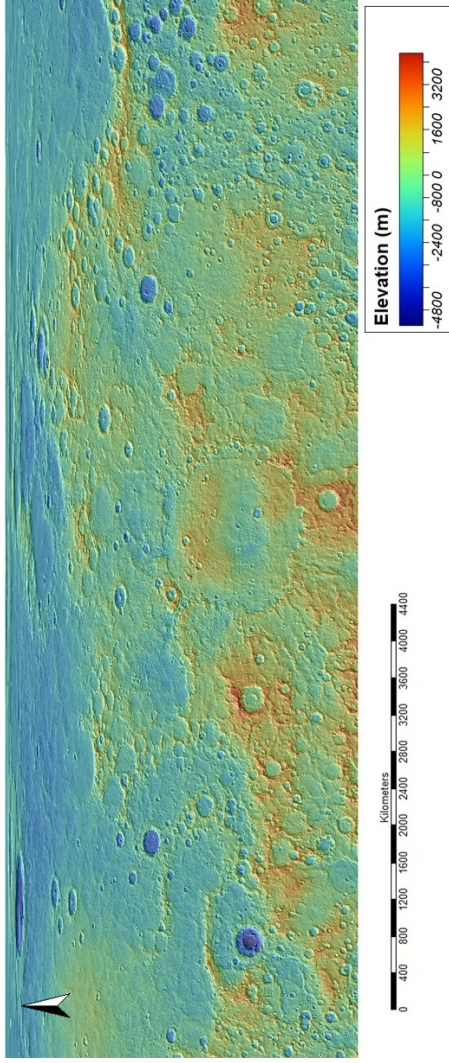


**Figure 5.** Spatial and frequency distribution of the DEM within the northern hemisphere of Mercury.

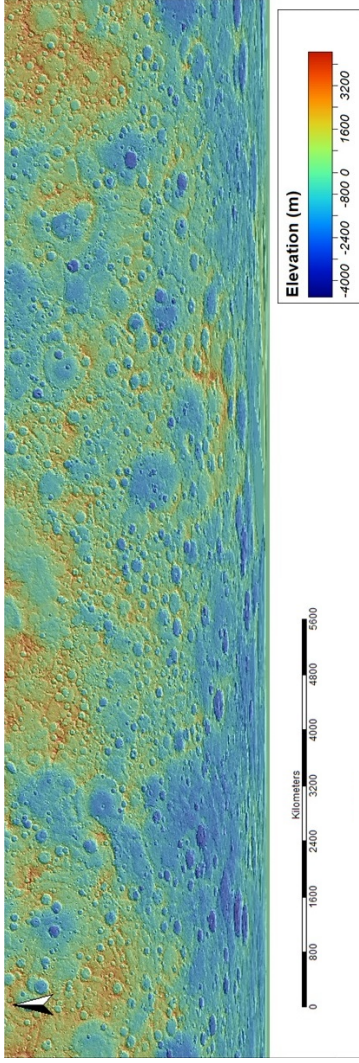


**Figure 6.** Spatial and frequency distribution of the DEM within the southern hemisphere of Mercury.

tains and ridges are localized up to  $30^{\circ} - 35^{\circ}$  northern and southern latitude, while the northern latitudes of the planet are predominantly represented by negative shapes and lowest values of gravity field.

In the course of the study, significant differences between Mercury's northern and southern hemispheres were found, both in terms of gravity and hypsometry. As we will see from the next section, these differences are well described by the variance of their fractal dimensions.

## Results and Discussion

The results obtained in the course of the study of Mercury's FAG and DEM fractal structure are summarized in Table 1. The main conclusions and interpretations are discussed further.

As we can see from the table, the FD min for both FAG and DEM in northern hemisphere is approximately equal. Vice versa – FD max are relatively different, but the tendencies are kept. In southern hemisphere FD max for DEM are larger (both for positive and negative values), but all values are similar in FD min. The  $R^2$  value is lower for the DEM of southern hemisphere. This indicated higher non-linearity in spatial distribu-

**Table 1.** Fractal Analysis of Mercury's FAG and DEM (Key: FD – Fractal Dimension;  $R^2$  – Coefficient of Determination)

Free-Air Gravity (FAG)						
Northern hemisphere			Southern hemisphere			
	All values	Positive	Negative	All values	Positive	Negative
FD min	2.10	2.01	2.01	2.13	2.01	2.01
FD max	2.56	2.38	2.41	2.64	2.40	2.44
$R^2$	0.908	0.968	0.967	0.975	0.994	0.990

Digital Elevation Model (DEM)						
Northern hemisphere			Southern hemisphere			
	All values	Positive	Negative	All values	Positive	Negative
FD min	2.01	2.0	2.01	2.01	2.0	2.01
FD max	2.64	2.45	2.58	2.58	2.47	2.54
$R^2$	0.942	0.903	0.940	0.857	0.863	0.910

tion of landforms to the south of Mercury. Within the southern hemisphere the transition from high to low landforms is clearly expressed. To the north, the positive and negative areas of the terrain are more compact and larger.

The comparison between the northern and southern hemisphere of FAG (positive and negative) anomalies (Figure 7 and Figure 8) shows clearly that the areas of both types of FAG anomalies dominated in their sizes and numbers. For example, the negative values in northern hemisphere have higher areas within range of FD between 2.36 and 2.40. For the southern hemisphere the same is true for the range between 2.37 and 2.40. Same tendency is clearly visual for the positive values.

The analysis of the FD for both hemispheres shows the following peculiarities: The fractal dimensions for both cases starts as values of 2 and finished at levels 2.4. Up to 2.27 (for northern hemisphere – NH) and 2.30 (to the southern one – SH) the fractal dimensions reflects both – positive and negative anomalies. These values show that in both cases the nonlinearity is clearly expressed but at almost the same values of areas (positive and negative). The appearance of some spikes in the distributions is not very clear and

will need additional investigations. After 2.27 (NH) and 2.30 (SH) the dynamics in the changes of FD's is sharper and rather specific for NH and SH. The FD of the positive anomalies in NH demonstrates a maximum between 2.37 and 2.38, which means specific fractal structure (i.e. fragmentation). The FD distribution of the positive anomalies in SH is unimodal, as well as both distributions of the FD's related to the negative anomalies. These specifics also need some additional investigations, but clearly confirm that the northern hemisphere is much more frequently attacked by the meteorites, asteroid and/or comets.

Generally within the northern hemisphere of Mercury  $R^2$  of fractal dimensions of both FAG and DEM are almost identical (Figure 7 and Figure 8), but this does not apply to the planet's southern hemisphere.

## **Conclusion**

The distributions of the DEM and FAG of northern and southern hemispheres of Mercury are studied. The results show clear fractal properties of the positive and negative areas of DEM and FAG. The correlation between them is confirmed. Sometimes there are some discrepancies in the correlation which probably means

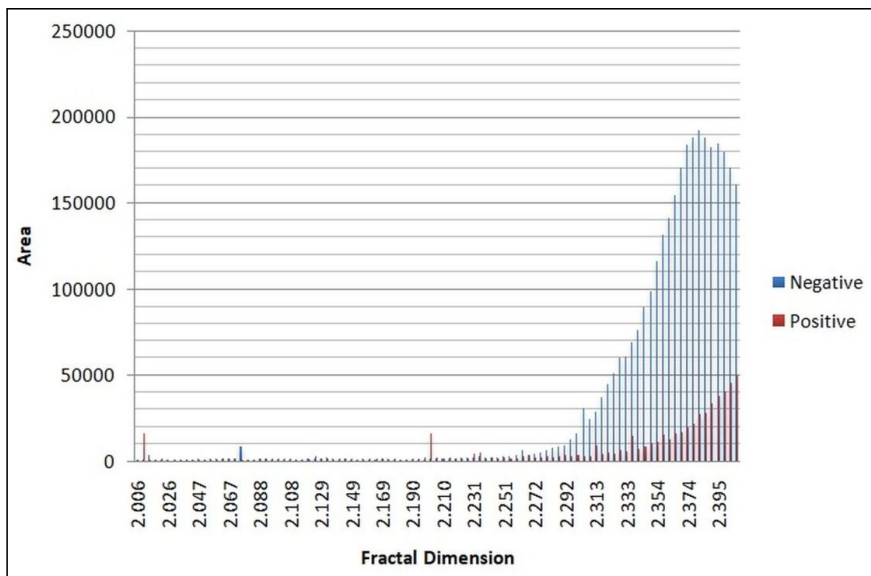


**Figure 7.** Fractal dimensions frequency of FAG positive and negative values within the northern hemisphere of Mercury.

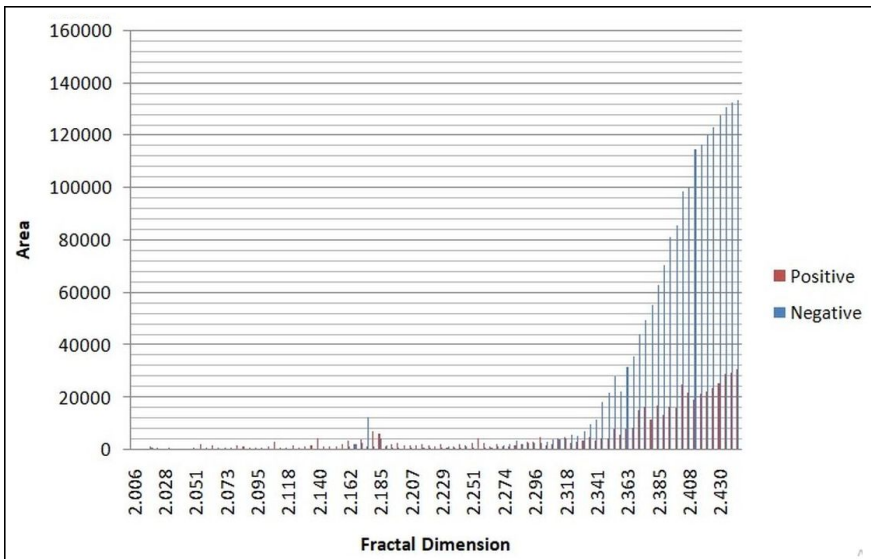


**Figure 8.** Fractal dimensions frequency of FAG positive and negative values within the southern hemisphere of Mercury.

lack of coincidence in the FAG and DEM due to the different densities.

The northern hemisphere is much more bombarded by meteorites and asteroids than the southern one. The fractal analysis confirmed this fact clearly. This means that the free space flying objects bombarding the Solar system dominated the North direction. If this is a space specific, it must be proved for other planetary objects in the Solar system too. The more dense free flying objects in the Solar system are about 1.5–2.0 times rarer than the less dense. It could be related to the physical properties of the meteorites and asteroids. Usually the less dense objects are identified as rocky objects, and the denser – as richer of metallic components space objects. This means that the “iron” objects (probably) are rarer within the Solar system. Probably it can be proved by the gravimetric studies to other terrestrial planets and satellites in the Solar system.

## References

Baldassarri, A., M. Montuori, O. Prieto-Ballesteros, S. C. Manrubia (2008) , Fractal properties of isolines at varying altitude revealing different dominant geological processes on Earth, *J.*

- Geophys. Res.*, 113, p. E09002, **Crossref**
- Becker, C. J., et al. (2016) , First Global Digital Elevation Model of Mercury, *47th Lunar and Planetary Science Conference, March 21–25, 2016, LPI Contribution No. 1903*, p. 2959, The Woodlands, Texas, USA.
- Bray, V. J., C. Atwood-Stone, C. D. Neish, et al. (2018) , Lobate impact melt flows within the extended ejecta blanket of Pierazzo crater, *Icarus*, 301, p. 26–36, **Crossref**
- Cao, W., Zh. Cai, Z. Tang (2015) , Fractal structure of lunar topography: An interpretation of topographic characteristics, *Geomorphology*, 238, p. 112–118, **Crossref**
- Conrad, O., et al. (2015) , System for Automated Geoscientific Analyses (SAGA) v. 2.1.4, *Geosci. Model Dev.*, 8, p. 1991–2007, **Crossref**
- Demin, S. A., A. O. Andreev, N. Y. Demina, Y. A. Nefediev (2017) , The fractal analysis of the gravitational field and topography of the Mars, *J. Phys.: Conf. Ser.*, 929 012002, p. 1–7, **Crossref**
- Demin, S. A., A. O. Andreev, N. Y. Demina, Y. A. Nefediev (2018) , The fractal analysis of the topography and gravitational field of Venus, *J. Phys.: Conf. Ser.*, 1038 012020, p. 1–6, **Crossref**
- Genova, A., et al. (2019) , Geodetic evidence that Mercury has a solid inner core, *Geophysical Research Letters*, p. 1–30, **Crossref**
- Huang, X., X. Jiang, T. Yu, H. Yin (2009) , Fractal-Based Lunar Terrain Surface Modeling for the Soft Landing Navigation, *Second International Conference on Intelligent Computation Tech-*

*nology and Automation*, p. 53–56, Changsha, Hunan, China, **Crossref**

Kumar, A. V. S., R. P. R. Sekhar, R. M. Tiwari (2016) , Fractal Analysis of lunar Gravity anomalies over the Basins of Lunar Farside, *19th National Space Science Symposium (NSSS-2016)*, Kerala, India, p. Poster Session, NSSS, Kerala, India.

Mancinelli, P., C. Pauselli, D. Perugini, A. Lupattelli, C. Federico (2014) , Fractal Dimension of Geologically Constrained Crater Populations of Mercury, *Pure and Applied Geophysics*, 172, no. 7, p. 1999–2008, **Crossref**

Mark, D. M., P. B. Aronson (1984) , Scale-Dependent fractal dimensions of topographic surfaces: An empirical investigation with applications in geomorphology and computer mapping, *Mathematical Geology*, 16, no. 7, p. 671–683, **Crossref**

Nefedjev, A. Y. (2003) , Lunar Surface Research Using Fractal Analysis, *Journal of the Eurasian Astronomical Society*, 22, no. 4–5, p. 631–632, **Crossref**

Pentland, A. P. (1984) , Fractal-based description of natural scenes, *IEEE Transactions on Pattern Analysis and Machine Intelligence*, PAMI-6, p. 661–674, **Crossref**

Rangelov, B., R. Iliev, Tz. Tzankov, E. Spassov (2019) , Fractal analysis of the lunar free-air gravity field, *Physics Journal*, 2, p. 126–133.

Rosenburg, M. A., et al. (2011) , Global surface slopes and roughness of the Moon from the Lunar Orbiter Laser Altimeter, *Journal of Geophysical Research*, 116, **Crossref**

Solomon, S. C., et al. (2001) , The MESSENGER mission to Mercury: Scientific objectives and implementation, *Planetary*

- and Space Science*, 49, no. 14–15, p. 1445–1465, **Crossref**
- Thiede, R., T. Sutton, H. Düster, M. Sutton (2014) , *Quantum GIS Training Manual*, 388 pp., Locate Press, Anchorage, USA.
- Turcotte, D. (1987) , A fractal interpretation of topography and geoid spectra on the Earth, moon, Venus, and Mars, *Journal of Geophysical Research*, 92, p. 597–601, **Crossref**
- Zhou, G., N. Lam (2005) , A comparison of fractal dimension estimator based on multiple surface generation algorithms, *Computers [ampersand] Geosciences*, 31, p. 1260–1269, **Crossref**
-